Photonic bandgap fiber bundle spectrometer

Qu Hang, Bora Ung, Imran Syed, Ning Guo, and Maksim Skorobogatiy*

Génie physique, Ecole Polytechnique de Montreal, C.P. 6079, succ.
Centre-ville, Montréal, Quebec, Canada, H3C 3A7

*Corresponding author: maksim.skorobogatiy@polymtl.ca

By using a photonic bandgap (PBG) fiber bundle and a monochrome CCD camera, we experimentally demonstrate an all-fiber spectrometer. A total of 100 Bragg fibers that have complementary and overlapping bandgaps are chosen to compose the fiber bundle. A monochrome CCD is then used to capture the binned image. To reconstruct the test spectrum from a single CCD image, we develop an algorithm based on pseudoinversion of the spectrometer transmission matrix. We demonstrate that the peak center wavelength can always be reconstructed within several percent of its true value regardless of the peak width or position, and that, although the widths of the individual Bragg fiber bandgaps are quite large (60–180 nm), the spectroscopic system has a resolution limit of ~30 nm. Moreover, we conclude that, by minimizing system errors, the resolution can be further improved down to several nanometers in width. Finally, we report fabrication of PBG fiber bundles containing hundreds of fibers using a two-stage drawing technique. This method constitutes a very promising approach toward industrial-strength fabrication of all-fiber spectrometers.   © 2010 Optical Society of America

OCIS codes: 060.5295, 120.6200, 060.2350.

1. Introduction

Development of multispectral imaging systems presents an active research field in rapid development. Inherent advantages of such systems include real-time monitoring, cost-effectiveness, and high accuracy. Imaging spectrometers have been demonstrated in many applications, including chemical component analysis [1], remote sensing [1,2], astronomy [3], and biochemistry [4]. Moreover, multispectral imaging systems have been successfully demonstrated both in the visible and the near-infrared spectral ranges [5–11].

An implementation of a multispectral imaging system can be realized by using a high-sensitivity, high signal-to-noise ratio photoelectric conversion device, such as a CCD array; optical filters or dispersive elements, which are either used to provide the reference spectra or to filter out a specific spectral component; as well as a broadband illuminant (light source). In such an imaging spectrometer, spectral information is acquired indirectly by taking several images in the complementary, while possibly overlapping, spectral ranges. A set of intensity images is then converted into spectra by utilizing various interpretation algorithms, such as pseudoinverse estimation, principal-component analysis, and nonlinear fitting [5,6]. In addition, the imaging Fourier transform spectrometer (IFTS), different from the above-mentioned implementation, is also widely used due to its high resolution. A traditional IFTS is realized by relaying a mechanically scanned Michelson interferometer to an imaging system. By scanning one of the mirrors in the interferometer, the optical path difference between the interferometer's two arms is varied. Thus, the interferograms are generated and interrogated by the imaging system. Applying Fourier transform on these interferograms will reconstruct the original spectrum.

Recently, several optical-fiber-based imaging spectrometers have been reported [7,8]. In [7], for example, the authors used, at the input end, a 10×10 bundle of mid-infrared fibers, which were then separated into a linear 1×100 array at the output end. The output beams were then simultaneously

dispersed using a single Bragg grating and imaged on a CCD array. This system, thus, functions as a 10×10 spectral imaging array. In another implementation [8], a multiple range spectrophotometer was implemented using an optical fiber probe. In that system, linear displacement of the light source was projected onto a fiber array (bundle) so that only a single fiber was lit for a given position of the light source. The fiber bundle was then interrogated using a spectrometer, thus enabling spatially resolved real-time data acquisition. Note that, in both examples, optical fibers were used exclusively as broadband optical guides, while a separate spectrometer was still required for the spectra acquisition.

Various fundamental properties of a spectrometer are encoded is its instrumental line shape function (ILSF), which can be used to deduce such performance parameters as spectral resolution, optical efficiency, and noise level. The spectrum acquired by the spectrometer is actually a convolution of the ILSF and the real spectra. The ILSF is affected by many factors, including the spectral acquisition approach and the mechanical alignment. For instance, the ILSF of a grating or a prism monochromator depends strongly on the widths of entrance and exit slits, the subcomponent dispersion, optical coupling efficiencies, aberrations in the setup optics, etc. As to the Fourier transform spectrometer, except for the instrument mechanical factors, the ILSF is also dependent on the Fourier transform algorithm used to resolve the interferograms [12], as well as on the other mathematical procedures, such as "apodization" or Fourier deconvolution [12–14], involved in the spectral calculations.

As we detail in what follows, our photonic bandgap (PBG) fiber bundle spectrometer realizes spectral reconstructions by interrogating the fiber bundle transmittances and then using a matrix pseudo inversion algorithm to reconstruct the original spectra. The ILSF of our fiber bundle spectrometer is, thus, mainly determined by the spectral reconstruction algorithm. Particularly, as we will see, the errors caused by the experimental noise can be multiplied by an ill-conditioned inversion procedure, thus affecting the ILSF of the fiber bundle spectrometer.

The goal of this paper is to demonstrate that the function of a spectrometer can be implemented directly inside a single fiber bundle. Then a complete imaging spectrometer can be realized by using an array of such fiber bundles interrogated by a linear or a two-dimensional (2D) CCD sensor. Such an approach would allow getting rid of costly and slow traditional spectrometers based on moving gratings, thus leading to significant cost savings and increased acquisition speed. Another advantage of our spectrometer is that its resolution is not dependent on the length of a fiber bundle. In fact, fiber bundles can be designed that are able to provide optical filtering over even centimeters-long lengths. This is in contrast with the grating-based spectrometer, whose resolution improves for longer optical paths traveled by light

inside of a spectrometer. In this paper we report for the first time, to our knowledge, a PBG-fiber-based spectrometer that consists of a photonic crystal fiber bundle and a monochrome CCD camera.

2. Characteristics of the Subcomponents: Bragg Fibers, Fiber Bundle, and CCD Camera

A. Photonic Bandgap Bragg Fibers

PBG fiber is a key element of our spectroscopic system. The PBG Bragg fibers used in the research are fabricated by our group and have been reported previously in [15–17]. An individual Bragg fiber features a large 300–700 μm diameter core made of a polymethyl methacrylate (PMMA) plastic. The core region is surrounded with a periodic multilayer reflector featuring ~100 submicrometer-thick layers of low and high refractive index PMMA/polystyrene (PS) plastics with refractive indices of 1.49/1.59. Such a multilayer (Bragg reflector) is responsible for the appearance of a spectrally narrow transmission band (reflector bandgap) within which the light is strongly confined inside the fiber core. For the wavelengths outside of the reflector bandgap, the light penetrates deeply into the multilayer region, exhibiting strong propagation loss due to scattering on the imperfections inside the multilayer region. A typical fiber loss within the reflector bandgap region is ~10 dB/m and is mostly determined by the bulk absorption loss of a low-purity PMMA plastic. Outside of a bandgap region, scattering loss (on the imperfections in the multilayer structure) dominates, resulting in >60 dB/m propagation loss. In our experiments, we used 30 cm long fibers so that the loss of guided light was below 3 dB, while the loss of nonguided light was >20 dB. The numerical aperture of all the Bragg fibers was in the range of 0.17–0.22.

To construct a fiber bundle spectrometer, we chose 100 Bragg fibers with complementary and partially overlapping bandgaps, as shown in Fig. 1(a). All the fibers in a bundle were drawn from the same preform, with the only difference among them being the final diameter. The smaller diameter fibers feature bandgaps shifted toward the blue part of a spectrum. This is easy to rationalize from the basic theory of Bragg fibers, which predicts that the bandgap center wavelength is proportional to the thickness of the multilayer in the Bragg reflector [18].

In Fig. 1(b), we also show distribution of the fiber transmission bandwidth as a function of the fiber transmission central wavelength. We note that the fiber transmission bandwidth increases with its center frequency. Thus, in the blue part of a spectrum, the fiber bandgap width is ~60 nm, while increasing to ~180 nm in the red part of a spectrum. There are two factors that contribute to this phenomenon. First, from the basic theory of Bragg fibers, it follows that the relative width of a PBG (ratio of the bandgap size to the bandgap center frequency) is mostly a function of the refractive index contrast in the Bragg fiber reflector [18,19]. As all the fibers used in this
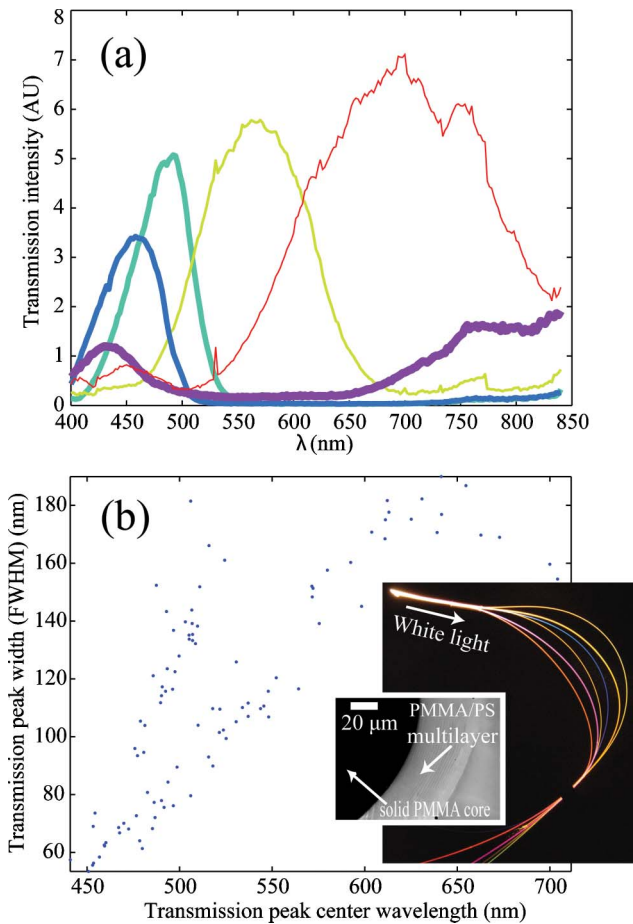
Fig. 1. (Color online) (a) Transmission spectra of five typical Bragg fibers used in the fiber bundle. (b) Distribution of the fiber transmission bandwidth as a function of the fiber bandgap center wavelength for all the Bragg fibers in a bundle. Inset, photo of a Bragg fiber cross section showing a solid core surrounded by a periodic multilayer reflector.

work are fabricated from the same preform, it means that the relative bandwidth is approximately constant for all the fibers, hence the absolute bandgap width should increase with the bandgap center frequency. Second, as we have mentioned in the previous paragraph, fibers featuring bandgaps at longer wavelengths have larger core size. In Bragg fibers, modal losses due to radiation and scattering on the reflector imperfections scale as $1/R^3$ with the core size. Therefore, larger core fibers exhibit smaller loss than smaller core fibers. Note that, in Fig. 1, we show the transmission intensities and not the actual losses. Clearly, for the fibers of the same length, smaller core fibers will exhibit spectrally narrower transmission, as wavelengths near the bandgap edge will be attenuated much more strongly than those in the larger core fibers.

B. Photonic Bandgap Fiber Bundle

The fiber bundle used in our experiments featured a 5.6 mm inner diameter plastic tube that hosted 100 Bragg fibers of 30 cm of length. Fibers at the input end of a bundle were rigidly attached with epoxy

to each other and to the confining tube, and the whole assembly was then polished using optical films of various granularity. On the other end of a bundle, 100 fibers were inserted into a custom-made block featuring holes of diameter 0.8 mm placed in a periodic 10×10 square array, see Fig. 2. The block, the tube, and all the fibers were bonded together with epoxy, and the output end was then polished.

The principle of operation of a PBG fiber bundle spectrometer can be clearly understood from Figs. 1 and 2. In principle, if all the fiber bandgaps were to be spectrally narrow and nonoverlapping, then, at the end of a fiber bundle, the relative intensities of light coming out of the individual fibers would be unambiguously related to the corresponding spectral components of an incoming light. In practice, individual fiber bandgaps are always overlapping and, in our particular implementation, the bandgaps are quite broad. Therefore, to reconstruct the intensity of an incoming light from the intensities of light coming out of the individual fibers of a bundle, we have to use a certain deconvolution algorithm. Note that spectrometer resolution is not directly limited by the width of fiber bandgaps. We study the resolution by testing a set of spectral peaks with bandwidth from 5 to 40 nm. As we will demonstrate in Section 5, even with all the individual bandgaps as wide as 60 nm, one could, in principle, reconstruct the peaks as narrow as 5–10 nm. However, to achieve such a high resolution, it is necessary to minimize the experimental errors and noise contributions.

Another important comment is about the intensity throughput of our spectrometer, and its relation to the spectrometer resolution. First of all, if all the fibers used in the spectrometer were to have strictly complementary (spectrally nonoverlapping) bandgaps of width $\delta\lambda$, then, to enable a certain spectrometer range $\Delta\lambda = (\lambda_{max} - \lambda_{min})$, one would need to
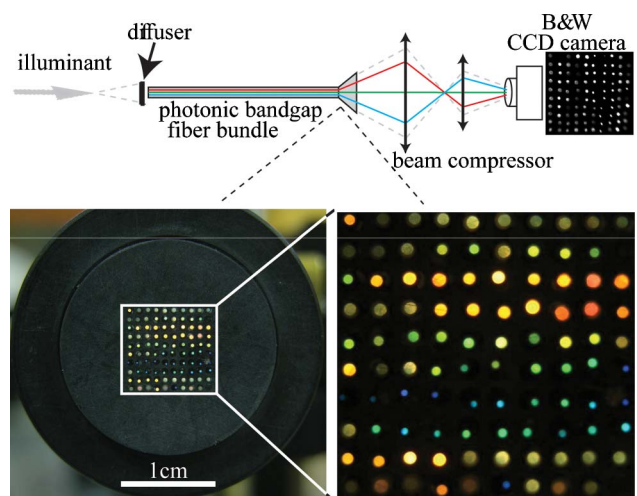

Fig. 2. (Color online) Fiber bundle spectrometer. Top, schematic of the spectrometer. Light from the illuminant is launched into the fiber bundle; the image is taken by the monochrome CCD. Bottom, when the broadband light is launched into the fiber bundle, the output is a mosaic of colors selected by the individual Bragg fibers.

use $N = \Delta\lambda/\delta\lambda$ fibers. Assuming a broadband light with a unit integral power in the spectral range $\Delta\lambda$, we conclude that the intensity throughput through such a spectrometer would be $\sim 1/N^2$. Indeed, the light beam first has to be physically divided into N parts to be launched into the individual fibers of a bundle; then, an individual fiber would cut out a spectrally narrow ($\sim 1/N$) part of the broadband light.

It is important to realize, that our implementation uses N Bragg fibers with relatively large and strongly overlapping bandgaps of spectral width $\delta\lambda \gg \Delta\lambda/N$. Spectral resolution of such a spectrometer can be still as small as $\Delta\lambda/N$, while the intensity throughput would be much higher and proportional to $1/N$, rather than $1/N^2$. Such intensity throughput is comparable to the throughput of a grating-based spectrometer with resolution of $\Delta\lambda/N$. Indeed, as we will see in what follows, because of the use of a pseudoinversion algorithm, the resolution of a fiber-based spectrometer is fundamentally limited only by the number of the spectroscopic elements, such as individual Bragg fibers, regardless of whether they feature overlapping or strictly complementary bandgaps. On the other hand, a throughput through an individual Bragg fiber with a relatively wide bandgap is $\delta\lambda/\Delta\lambda \gg 1/N$, and is no longer limited by the resolution. The overall $1/N$ scaling of the throughput intensity, therefore, mostly comes from the necessity of subdivision of a test beam into N individual fibers, each of which individually transmits as much as 30%–50% of the in-coupled intensity. In practice, achieving $\Delta\lambda/N$ resolution with N fibers featuring overlapping bandgaps is somewhat challenging, as a pseudoinverse algorithm used in the spectrum reconstruction is sensitive to the experimental errors.

C. Sensitivity and Linear Response of a CCD Sensor

The output of the fiber bundle is a 10×10 matrix of colored fibers, which is then projected with a beam compressor onto a monochrome CCD array (see Fig. 2). The sensitivity of a CCD sensor would directly affect the measuring range, the signal-to-noise ratio, and the algorithm that we use to reconstruct the spectrum of an illuminant. The CCD sensor in our experiment is an Opteon Depict 1, E and S Series B1A 652×494 black and white CCD. The normalized sensitivity for different wavelengths is displayed in Fig. 3(a), from which it is clear that the sensor covers well all the visible and a part of a near-infrared spectral range. The sensitivity curve, however, is a highly variable function of wavelength, which must be taken into account in the reconstruction algorithm. Figure 3(a) was obtained by launching the light from a supercontinuum source into a monochromator whose output would produce a 2 nm wide (FWHM) peak at a desired center wavelength. Light from such a tunable source would then be launched into a commercial multimode fiber of ~ 1 mm diameter. The output power from such a fiber would then be
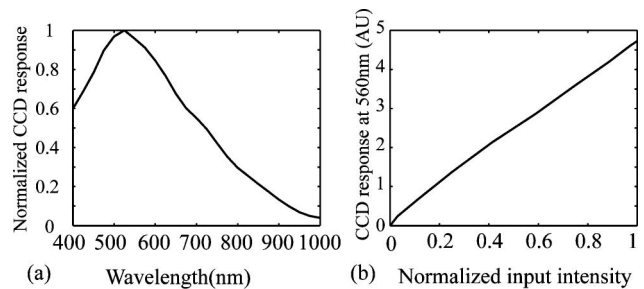

Fig. 3. (a) Normalized spectral response of a CCD array. (b) Typical monochromatic near-linear response of a CCD array ($\lambda = 560$ nm).

measured by both the CCD array and a calibrated powermeter; the sensitivity curve is then achieved by dividing one by the other.

As we will see in Subsection 3.A, one of the key requirements of a CCD array is linearity of its monochromatic response as a function of the intensity of incident light. The near-linear response of a CCD sensor was confirmed at several wavelengths of interest; a typical CCD response (at $\lambda = 560$ nm) is presented in Fig. 3(b). To obtain Fig. 3(b), two polarizers were placed between a CCD array and the output of a commercial fiber in a setup described in the previous paragraph. By varying the angle between the two polarizers, we also varied the intensity of light coming onto a CCD array. A reference measurement is performed with a calibrated powermeter for the same angles between polarizers; the results are compared to establish a near-linear sensor response.

3. Calibration of the Fiber Bundle Spectrometer and Spectrum Reconstruction Algorithm

In its operation mode, the fiber bundle spectrometer is illuminated with a test light, which is then spectrally and spatially decomposed by the fiber bundle (see Fig. 4). The test spectra used in our experiments were either broadband (halogen lamp source), or narrow-band (tunable monochromator source). The image of the fiber bundle output end was then projected onto a monochrome CCD array using a 2:1 beam compressor. Note that a CCD array does not have to be a 2D camera; instead, one can use an
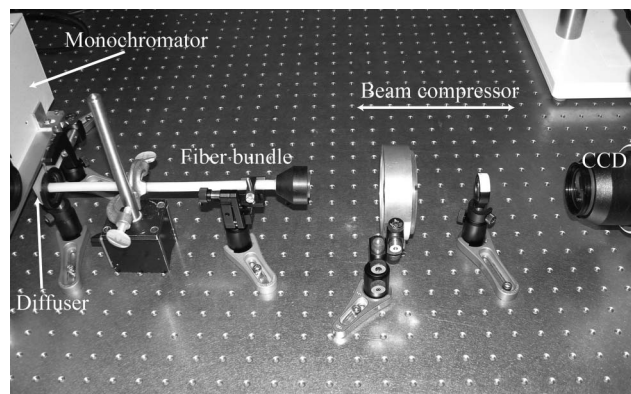

Fig. 4. Setup for the spectrometer calibration measurement.

economical linear array with the number of pixels matching the number of Bragg fibers in a bundle. The output of each fiber carries information about the intensity of a certain fraction of an illuminant spectrum as filtered by the individual Bragg fibers. It is reasonable to assume, then, that if the Bragg fibers of a bundle feature complementary, while possibly overlapping, bandgaps that together cover the spectral range of interest, then the spectrum of an illuminant could be reconstructed.

A. Transmission Matrix Method

To interpret a monochrome CCD image, we use a so-called luminance adaptation model of the fiber spectrometer. Particularly, for a fixed exposure time of a CCD array, total intensity C_n registered by an assigned region of a CCD sensor from the output of the nth fiber can be presented as

$$C_n = \int_{\lambda_{\min}}^{\lambda_{\max}} I(\lambda) A_n F_n(\lambda) S(\lambda) O_n(\lambda) d\lambda, \qquad (1)$$

where $I(\lambda)$ is the illuminant spectral flux density at the fiber bundle input end, A_n is the area of the nth fiber input cross section, $F_n(\lambda)$ is the transmission function of the nth fiber, $S(\lambda)$ is the spectral sensitivity of a CCD array, and $O_n(\lambda)$ is a fiber-position-dependent transmission function of various optics (diffuser, beam compressor, and a CCD objective). Measuring such transmission functions individually is a daunting task. Instead, we use a calibration procedure that measures a compounded transmission matrix of our spectrometer, defined as $T_n(\lambda) = A_n F_n(\lambda) S(\lambda) O_n(\lambda)$. The model in Eq. (1) could then be rewritten as

$$\begin{aligned} C_n &= \int_{\lambda_{\min}}^{\lambda_{\max}} I(\lambda) T_n(\lambda) d\lambda \\ &= \sum_{i=0,\lambda_i=\lambda_{\min}+i\Delta\lambda}^{N=(\lambda_{\max}-\lambda_{\min})/\Delta\lambda} T_n(\lambda_i) \int_{\lambda_i}^{\lambda_i+\Delta\lambda} I(\lambda) d\lambda = \sum_{i=0}^{N} I_i \cdot T_n^i. \end{aligned}$$
$$(2)$$

Experimentally, the integral in Eq. (2) is rather a sum over the intensity contributions from small spectral "bins" of size $\Delta\lambda$. Equation (2) presented in matrix form becomes

$$\begin{bmatrix} C_1 \\ \vdots \\ C_{100} \end{bmatrix} = \begin{bmatrix} T_{1,1} & \cdots & T_{1,N} \\ \vdots & \ddots & \vdots \\ T_{100,1} & \cdots & T_{100,N} \end{bmatrix} \begin{bmatrix} I_1 \\ \vdots \\ I_N \end{bmatrix}, \qquad (3)$$

where vector $(C)_{100\times1}$ represents the intensities of light coming out of the individual fibers as measured by the CCD sensor, $(T)_{100\times N}$ is a spectrometer transmission matrix, and $(I)_{N\times1}$ is a discretized spectrum of the illuminant. From Eq. (3) it follows that a discretized spectrum of the illuminant can be reconstructed from the corresponding CCD image (C vector) by inverting the transmission matrix of a spectrometer.

B. Calibration Measurement, Building a Transmission Matrix

To construct transmission matrix experimentally we note that, if the illuminant spectrum is monochromatic [$I_i = 0$, $\forall i \neq i_\lambda$ in Eq. (3)], then the measured C^{i_λ} vector is proportional to the i_λ column of the transmission matrix:

$$C^{i_\lambda}(1:100) = T(1:100, i_\lambda) \cdot I_{i_\lambda}. \qquad (4)$$

To construct the transmission matrix experimentally we use a tunable monochromator-based narrowband (2 nm FWHM) source to generated "monochromatic" spectra (see Fig. 4). Particularly, we vary the source center wavelength in 2 nm increments, thus effectively subdividing the 400–840 nm spectral interval under consideration into $N = 221$ equivalent 2 nm wide bins. For every new position of the source center wavelength, we acquire a C vector using a CCD array and consider it as the next column of the spectrometer transmission matrix. Finally, to finish calibration, we measure the wavelength-dependent intensities I_i of a tunable source by placing a calibrated powermeter directly at the output of a monochromator. By dividing every C vector by the corresponding I_i value, the transmission matrix is constructed.

In our experiments, an S&Y halogen lamp source was used with a Newport Oriel 1/8 m monochromator to build a narrowband tunable source of 2.0 nm FWHM (see Fig. 4). The light beam from the source was then directed onto a diffuser placed right before the fiber bundle to guarantee a uniform illumination of its input end. At the output end of a fiber bundle, a 2:1 beam compressor was used to image the fiber bundle output facet onto the 8 bit monochrome CCD sensor array. Individual images were then interpreted using a singular value decomposition (SVD) pseudoinversion algorithm to construct the corresponding C vectors. The wavelength-dependent intensity of a tunable source was measured using a calibrated Newport 841-PE powermeter.

C. Spectral Reconstruction Algorithm

As it was noted in Subsection 3.A, a discretized spectrum of the illuminant can be reconstructed from the corresponding CCD image (C vector) by inverting the transmission matrix of a spectrometer in Eq. (3). However, an immediate problem that one encounters when trying to invert the transmission matrix is that the matrix is nonsquare. Even if the number of spectral bins is chosen to match the number of fibers in the bundle, thus resulting in a square transmission matrix, one finds that such a matrix is ill-conditioned. One, therefore, has to resort to an approximate inverse of a transmission matrix. To find a pseudoinverse of a transmission matrix in

Eq. (3), we employ a SVD algorithm. Particularly, from linear algebra, we know that any $(100 \times N)$ matrix (suppose that $N > 100$) can be presented in the form

$$(T)_{100 \times N} = (U)_{100 \times 100}(S)_{100 \times N}(V^T)_{N \times N}, \qquad U^T U = 1;$$
$$V^T V = 1; \qquad S = \text{diag}(\sigma_1, \sigma_2, \sigma_3, \ldots \sigma_{100}),$$
$$\sigma_1 > \sigma_2 > \sigma_3 > \ldots > \sigma_{100} > 0, \tag{5}$$

where matrices U and V are unitary, and matrix S is a diagonal matrix of the real positive singular values. For the ill-conditioned matrices, most of the singular values are small and can be taken as zero. By limiting the number of nonzero singular values to N_σ, Eq. (5) can be rewritten as

$$(T)_{100 \times N} = (U)_{100 \times N_\sigma}(S)_{N_\sigma \times N_\sigma}(V^T)_{N_\sigma \times N},$$
$$\sigma_1, \sigma_2, \ldots, \sigma_{N_\sigma} \neq 0, \tag{6}$$

and a corresponding pseudoinverse of the transmission matrix is then found as

$$(T)^{-1}_{N \times 100} = (V)_{N \times N_\sigma}(S)^{-1}_{N_\sigma \times N_\sigma}(U^T)_{N_\sigma \times 100}. \tag{7}$$

4. Experimental Results

To test our fiber bundle spectrometer, we perform reconstruction of several test spectra. In one set of experiments, the test spectra is a set of the 25 nm wide peaks centered at 450, 500, 550, 600, and 700 nm. Such peaks were created using the same monochromator-based tunable source as was used for the spectrometer calibration; however, it was adjusted to have a 25 nm bandwidth of the outgoing light. In the second set of experiments, we measure the spectra of four 40 nm wide bell-shaped curves centered at 450, 500, 550, and 600 nm created by using four commercial bandpass filters. In Fig. 5 we demonstrate, with dashed curves, the test spectra of light beams at the input of a fiber bundle (as resolved by another Oriel monochromator), while with solid curves, we show the corresponding reconstructed spectra using the transmission matrix inversion algorithm. In the figures, we also indicate the optimal number of nonzero singular values used in the matrix inversion procedure (7). The choice of the number of nonzero singular values used in the spectrum reconstruction algorithm affects strongly the quality of the reconstructed spectrum. Note, in particular, that although the spectral intensity function should be strictly nonnegative, the reconstructed spectral intensity can take negative values. Therefore, spectrum reconstruction error can be defined as the ratio of the most negative value of the reconstructed spectral intensity to its most positive value:

$$\text{Error}(N_\sigma) = -\min_\lambda(I^{\text{reconstr.}}_{N_\sigma})/\max_\lambda(I^{\text{reconstr.}}_{N_\sigma}), \tag{8}$$

and the optimal N_σ to be used in Eq. (7) is the one that minimizes the error (8).

From Fig. 5 we conclude that the test peak position (the value of the peak center wavelength) can be reconstructed within several percent of its true value in the whole spectral range covered by the spectrometer. Moreover, we note that, although the widths of the individual Bragg fiber bandgaps are quite large (>60 nm), the fiber-bundle-based spectroscopic system can resolve peaks of much smaller spectral width. Indeed, in Fig. 5(a), the widths of the reconstructed spectra are in the 30–50 nm range, with the exception of a peak centered at 600 nm. We mention in passing that we have also conducted measurements using 5, 10, 15, and 20 nm wide peaks. In all the experiments, we saw that the center wavelength of even the narrowest peak can be reconstructed with high precision; however, the reconstructed peak width always stayed around 30 nm. Finally, 40 nm wide test peaks could be well reconstructed, in terms of both their spectral positions and widths [see Fig. 5(b)].
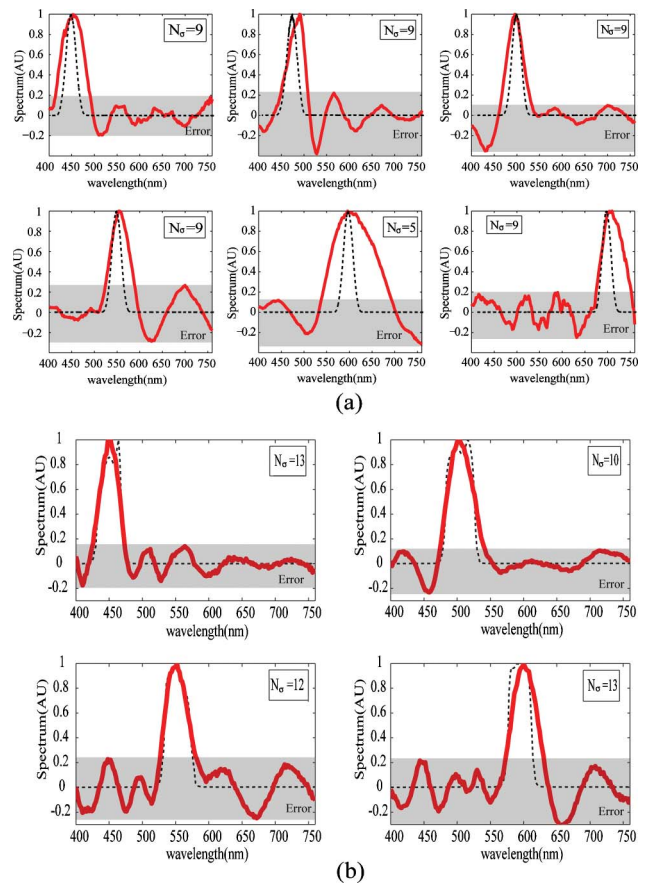

Fig. 5. (Color online) Spectra reconstruction using PBG fiber-bundle-based spectrometer. (a) Reconstructed spectra of six 25 nm wide peaks. (b) Reconstructed spectra of four 40 nm wide bell-shaped spectra. The black dashed lines are the test spectra resolved by another monochromator; the red solid curves are the spectra reconstructed by the fiber bundle spectrometer. The gray area indicates the error level.

5. Spectral Resolution Limit for the Fiber-Bundle-Based Spectrometer

To understand the resolution limit of our spectrometer, we first study the effect of the choice of the number of nonzero singular values N_σ used in the inversion algorithm of Eq. (7). At first, we assume that there is no noise in the system. As a test spectrum $I(\lambda)$, we consider a 20 nm wide peak centered at the wavelength of 520 nm [dashed curve in Fig. 6(a)].

We then multiply the discretized test spectrum by the transmission matrix of our spectrometer (measured experimentally), and then reconstruct the test spectrum by using a transmission matrix pseudoinverse with N_σ singular values:

$$(C)_{100\times1} = (T)_{100\times N}(I)_{N\times1},$$
$$(I_{N_\sigma}^{\text{reconstr.}})_{N\times1} = (V)_{N\times N_\sigma}(S)_{N_\sigma\times N_\sigma}^{-1}(U^T)_{N_\sigma\times100}(C)_{100\times1}.$$
$$(9)$$

The thus reconstructed spectrum is then compared to the original test spectrum. In Fig. 6(a), we present several reconstructed spectra for the different numbers of singular values used in the inversion algorithm. If all the 100 singular values are used [curve labeled $N_\sigma = 100$ in Fig. 6(a)], then the 20 nm wide peak is very well reconstructed, featuring a less

than 5% intensity difference with the reconstructed spectrum. The error manifests itself in the form of ripples at the peak tails. When a smaller number of singular values are used [for example, $N_\sigma = 10$ curve in Fig. 6(a)], the center wavelength of the reconstructed peak still coincides very well with that of a test peak; however, the reconstructed peak width is larger than that of a narrow test peak. This result is easy to understand by remembering that the expansion basis set used in the reconstruction algorithm is formed by the relatively broad (>60 nm; see Fig. 1) transmission spectra of the Bragg fibers; therefore, one needs a large number of such basis functions (singular values) to reconstruct a narrow spectral feature. In Fig. 6(b), the FWHM of the reconstructed peak is shown as a function of the number of singular values used in the matrix inversion. Note that more than 40 singular values have to be used to achieve the width of a reconstructed peak to be close to the 20 nm width of a test peak. When only ten singular values are used, the width of a reconstructed peak increases to 40 nm. Additionally, the peak reconstruction error as defined by Eq. (8) increases to 20% when a small number of singular values $N_\sigma < 20$ is used. From this we conclude that, with no noise present in the system, the peak reconstruction error and the quality of a reconstructed spectrum improves when a larger number of singular values is used.

We now study the effect of experimental noise on the quality of a reconstructed spectrum. There are several sources of noise in our spectrometer. One is the discrete intensity resolution of a CCD array; with the 8 bit encoding, the fundamental noise is $\sim0.1\%$. The ambient light in the experimental environment also contributes to noise on a CCD sensor. Moreover, because of the relatively large size of a fiber bundle (~6 mm), it is difficult to ensure the same illumination conditions of the bundle input facet for all the sources used in the experiments.

To model experimental noise numerically, we first multiply the test spectrum by the transmission matrix of our spectrometer, then add a uniformly distributed random noise of the relative intensity δ to the C vector (monochrome image), and finally, we reconstruct the test spectrum by using a transmission matrix pseudoinverse with N_σ singular values:
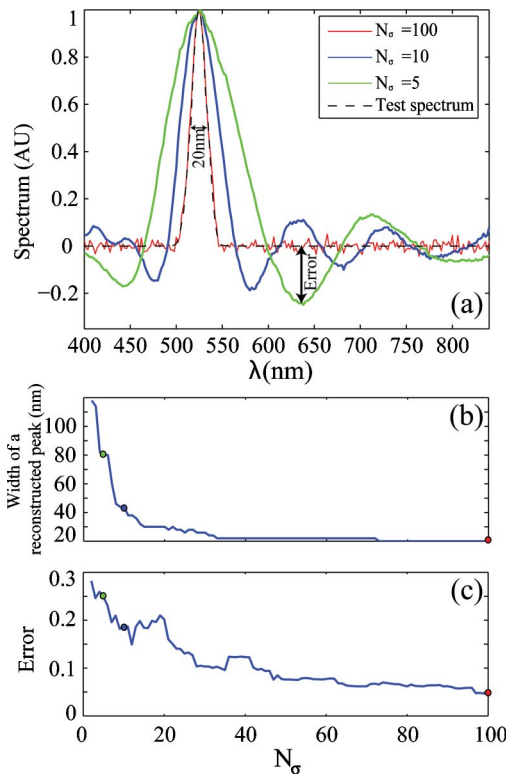

Fig. 6. (Color online) Properties of the reconstructed spectra as a function of the number of singular values used in the inversion algorithm. No noise is present in the system. (a) Dependence of the spectral shape of a reconstructed peak on N_σ. (b) Width of a reconstructed peak as a function of N_σ. (c) Reconstruction error as a function of N_σ.

$$(C)_{100\times1} = (T)_{100\times N}(I)_{N\times1},$$
$$(C^{\text{noise}})_{100\times1} = (C)_{100\times1} \cdot (1 + \delta \cdot (\eta)_{100\times1});$$
$$\eta - \text{random} \subset [-0.5, 0.5],$$
$$(I_{N_\sigma}^{\text{reconstr.}})_{N\times1} = (V)_{N\times N_\sigma}(S)_{N_\sigma\times N_\sigma}^{-1}(U^T)_{N_\sigma\times100}(C^{\text{noise}})_{100\times1}.$$
$$(10)$$

With these definitions, we first revisit the case when all the 100 singular values are used for spectrum reconstruction. As noted above, in the absence of noise [$\delta = 0$ in Fig. 7(i)], the 20 nm peak can be well reconstructed with only $\sim5\%$ error. However, the addition

of even a small amount of noise [$\delta = 0.005$ in Fig. 7 (ii)] results in a highly noisy reconstructed image, with errors as large as 50%. Note that, by using a smaller number of singular values $N_\sigma \subset [20, 40]$ (see the error plot in the top part of Fig. 7), the error of peak reconstruction can be greatly reduced, to 10%, while still allowing a fair estimate of the peak width ~ 30 nm. When the noise level is increased further, to avoid large reconstruction errors, one has to use a relatively small number of singular values $N_\sigma < 20$ [see Figs. 7(iii,iv)]. Notably, reconstruction error saturates at 20% even for large noise levels; however, the reconstructed peak width stays always larger than 30 nm due to a small number of singular values used.

To put the noise value of $\delta = 0.005$ into perspective, we note that this correspond to a 0.5% total experimental error in the amplitude measurement of the C vector components. The noises in measuring a C vector include the quantization noise of the CCD sensor, the ambient light contribution from the experimental environment, the measurement-to-measurement variation in the illumination conditions on the input facet of the fiber bundle, etc. As noted before, the contribution of quantization noise is $\sim 0.1\%$. We have verified that the ambient light noise is below 1 unit in the 8 bit coding, while the CCD sensor was configured so that the maximum of the fiber output is close to (but smaller than) 256 units per pixel. Thus, the ambient light noise

is limited by $1/256 = 0.39\%$. Thus, $\delta = 0.005$ is based on the assumption that only ambient light noise and quantization noise exist in the measurement of the C vector, while for other, higher δ, the other types of noise gradually become dominant. We find that the biggest contribution to noise is caused by the difficulty in reproducing the same illumination conditions of the fiber bundle facet when constructing the transfer matrix, and when characterizing the test spectra. The main reason for this is that, to construct the spectrometer transfer matrix, we use a monochromator-based source, while for the test spectra, we use a halogen lamp source. Because of the relatively large size of a fiber bundle, it is then difficult to guarantee consistent illumination of the fiber bundle surface, even when using a diffuser in front of the fiber bundle. An obvious remedy to this problem is to reduce the size of the fiber bundle and to use a better diffuser, or mode scrambler, at the input. To address the first problems, we report in Section 6 a new fabrication technique where a smaller size fiber bundle is fabricated by direct drawing. Additionally, several-meter-long large-core multimode fiber can be used to first scramble and equalize polarization and incident angle distributions of the input light, and then launch the scrambled light into the fiber bundle.

Finally, Fig. 8 presents statistical averages of various parameters (thick solid curves), as well as their statistical deviation from the average (thin dashed curves) as a function of the noise level. To construct these curves, for every value of the noise amplitude δ, we first generate 200 realizations of noise. Then, for every realization of noise, we plot the error of peak reconstruction as a function of the number of singular values (similar to Fig. 7). Last, the smallest error, the corresponding N_σ, and the width of a reconstructed peak are recorded and statistical averages are performed. In Fig. 8(a), we present the average peak reconstruction error as a function of the noise amplitude. Note that, although the error grows with the noise amplitude, it nevertheless saturates at $\sim 20\%$, even for large noise levels. In the inset of Fig. 8(a), we see that, at very small noise levels ($\delta < 0.02$), to obtain the smallest reconstruction error one can use almost all 100 singular values, while at higher noise levels, fewer than 20 singular values should be used. As a consequence, for larger noise amplitudes, the width of a reconstructed peak could become considerably larger than that of a test peak (20 nm).
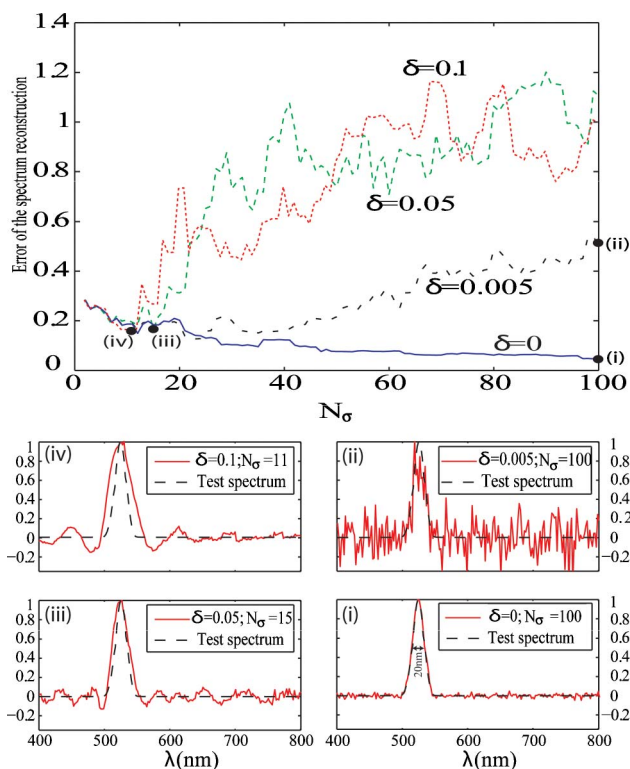

Fig. 7. (Color online) Effect of noise on the quality of reconstruction. Examples of the reconstructed spectra for several particular realizations of noise with amplitudes (i) $\delta = 0$, (ii) $\delta = 0.005$, (iii) $\delta = 0.05$, and (iv) $\delta = 0.1$.

6. Novel Technique for Drawing PBG Fiber Bundles

Finally, we report a two-stage drawing technique for direct fabrication of the PBG fiber bundles. This technique constitutes an industrial-strength alternative to the manual bundling of the individual fibers, as it was presented in Subsection 2.B. The proposed technique comprises "two stages." First, we produce a Bragg fiber preform by a co-rolling technique [20] and draw it into intermediate preforms with relatively large and variable diameters (1–1.5 mm).
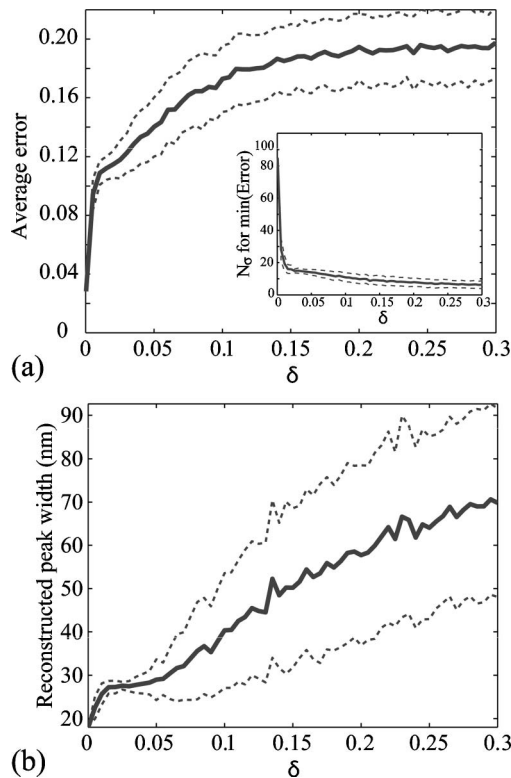
Fig. 8. Effect of noise on the reconstruction algorithm. (a) Average reconstruction error and its statistical deviation as a function of the noise amplitude. Inset, optimal number of singular values needed to minimize the reconstruction error. (b) Average width of a reconstructed peak and its statistical deviation as a function of the noise level.

Second, we bundle these intermediate preforms, place them into a thin supercladding tube, and, finally, draw this structure into a PBG fiber bundle. An example of a cross section of a PBG fiber bundle is presented in Fig. 9. It is a 3.8 mm diameter fiber bundle that contains ~100 Bragg fibers featuring complementary bandgaps. At the input end of the bundle we use white light, which is then split by the individual fibers into the respective spectral
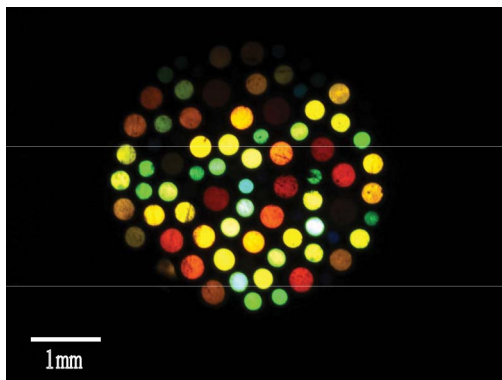

Fig. 9. (Color online) Cross section of a fiber bundle fabricated using the two-stage drawing technique. The bundle is illuminated with a wideband halogen lamp source. At the fiber bundle output, a mosaic of colors is visible as the white light is split into the various spectral components.

components, as seen in Fig. 9. We are currently working on the perfection of this fiber bundle fabrication technique to include more fibers, and to reduce the bundle outer diameter in order to demonstrate compact and high-resolution spectrometers that are also resistant to experimental noise.

7. Conclusion

We have demonstrated experimentally a novel all-fiber spectrometer comprising a PBG fiber bundle and a monochrome CCD camera. One hundred Bragg fibers with complementary bandgaps covering a 400–840 nm spectral range were placed together to make a ~6 mm in diameter, 30 cm long fiber bundle. The spectrometer operates by launching the light into a fiber bundle and then recording the color-separated image at the fiber bundle output facet using a CCD camera. An inversion algorithm was developed to reconstruct the test spectrum by using black and white intensity images. Among the clear advantages of our spectrometer is the lack of moving parts, a near-instantaneous and parallel acquisition of all the spectral components, compactness, a high degree of integration, and simplicity of operation, as well as a relatively high throughput.

The PBG fiber bundle spectrometer was demonstrated experimentally to resolve relatively narrow spectral peaks (5–40 nm) with high precision in determining the position of the peak center wavelength. Even when the peak width was much narrower than the bandwidth of the individual Bragg fibers making up the fiber bundle, the peak width could still be resolved correctly; however, the reconstruction algorithm was found to be sensitive to experimental noise. The experimental resolution limit of the fiber bundle spectrometer presented in this paper is found to be ~30 nm. Theoretical analysis predicts that the resolution limit of the existing setup could be greatly improved by (1) minimizing the experimental errors related to repeatability of light injection into the bundle, (2) optical isolation of the bundle from the environment, and (3) minimizing discretization errors introduced by the camera. Finally, we demonstrate a two-stage industrial-strength drawing technique suitable for the mass production of the PBG fiber bundles.

References

1. S. M. Ramasamy, V. Venkatasubrmanian, and S. Anbazhagan, "Reflectance spectra of minerals and their discrimination using Thematic Mapper, IRS and SPOT multispectral data," Int. J. Remote Sens. **14**, 2935–2970 (1993).
2. G. Vane and A. F. H. Goetz, "Terrestrial imaging spectroscopy," Remote Sens. Environ. **24**, 1–29 (1988).
3. A. Rosselet, W. Graff, U. P. Wild, and R. Gshwind, "Persistent spectral hole burning used for spectrally high-resolved imaging of the sun," Proc. SPIE **2480**, 205–212 (1995).
4. D. L. Farkas, B. T. Ballow, G. W. Fisher, W. Niu, and E. S. Wachman, "Microscopic and mesoscopic spectral bio-imaging," Proc. SPIE **2678**, 200–206 (1996).
5. M. Vilaseca, J. Pujol, and M. Arjona, "Multispectral system for reflectance reconstruction in the near-infrared region," Appl. Opt. **45**, 4241–4253 (2006).

6. M. Vilaseca, J. Pujol, and M. Arjona, "Spectral-reflectance reconstruction in the near-infrared region by use of conventional charge-coupled-device camera measurements," Appl. Opt. **42**, 1788–1798 (2003).

7. H. Suto, "Chalcogenide fiber bundle for 3D spectroscopy," Infrared Phys. Technol. **38**, 93–99 (1997).

8. B. Lienert, J. Porter, and S. K. Sharma, "Simultaneous measurement of spectra at multiple ranges using a single spectrometer," Appl. Opt. **48**, 4762–4766 (2009).

9. J. Y. Hardeberg, F. Schmitt, and H. Brettel, "Multispectral image capture using a liquid crystal tunable filter," Opt. Eng. **41**, 2532–2548 (2002).

10. J. Y. Hardegerg, F. Schmitt, H. Brettel, J. Crettez, and H. Maitre, "Multispectral image acquisition and simulation of illuminant changes," in *Colour Imaging: Vision and Technology*, L. W. MacDonald and M. R. Luo, eds (Wiley, 1999), pp. 145–164.

11. M. H. Kasari, "Spectral vision system for measuring color images," J. Opt. Soc. Am. A **16**, 2352–2362 (1999).

12. R. J. Bell, *Introductory Fourier Transform Spectroscopy* (Academic, 1972), pp 56–60.

13. F. Hase, T. Blumenstock, and C. Paton-Walsh, "Analysis of the instrumental line shape of high-resolution Fourier transform IR spectrometers with gas cell measurements and new retrieval software," Appl. Opt. **38**, 3417–3422 (1999).

14. C. Bernardo and D. W. T. Griffith, "Fourier transform spectrometer instrumental lineshape (ILS) retrieval by Fourier deconvolution," J. Quant. Spectrosc. Radiat. Transfer **95**, 141–150 (2005).

15. M. Skorobogatiy and N. Guo, "Bandwidth enhancement by differential mode attenuation in multimode photonic crystal Bragg fibers," Opt. Lett. **32**, 900–902 (2007).

16. A. Dupuis, N. Guo, B. Gauvreau, A. Hassani, E. Pone, F. Boismenu, and M. Skorobogatiy, "Guiding in the visible with "colorful" solid-core Bragg fibers," Opt. Lett. **32**, 2882–2884 (2007).

17. B. Gauvreau, N. Guo, K. Schicker, K. Stoeffler, F. Boismenu, A. Ajji, R. Wingfield, C. Dubois, and M. Skorobogatiy, "Color-changing and color-tunable photonic bandgap fiber textiles," Opt. Express **16**, 15677–15693 (2008).

18. S. G. Johnson, M. Ibanescu, M. Skorobogatiy, O. Weisberg, T. D. Engeness, M. Solljacic, S. A. Jacobs, J. D. Joannopoulos, and Y. Fink, "Low-loss asymptotically single-mode propagation in large-core OmniGuide fiber," Opt. Express **9**, 748–779 (2001).

19. M. Skorobogatiy and A. Dupuis, "Ferroelectric all-polymer hollow Bragg fibers for terahertz guidance," Appl. Phys. Lett. **90**, 113514 (2007).

20. Y. Gao, N. Guo, B. Gauvreau, M. Rajabian, O. Skorobogata, E. Pone, O. Zabeida, L. Martinu, C. Dubois, and M. Skorobogatiy, "Consecutive solvent evaporation and co-rolling technique for polymer multilayer hollow fiber preform fabrication," J. Mater. Res. **21**, 2246–2254 (2006).